J. Fluid Mech. (2006), *vol.* 548, *pp.* 87–111.
doi:10.1017/S0022112005007494 Printed in the United Kingdom

Onset of convection in a gravitationally unstable diffusive boundary layer in porous media

By A. RIAZ, M. HESSE, H. A. TCHELEPI† AND F. M. ORR JR

Department of Petroleum Engineering, Stanford University, Stanford, CA 94305, USA

(Received 30 March 2005 and in revised form 22 July 2005)

We present a linear stability analysis of density-driven miscible flow in porous media in the context of carbon dioxide sequestration in saline aquifers. Carbon dioxide dissolution into the underlying brine leads to a local density increase that results in a gravitational instability. The physical phenomenon is analogous to the thermal convective instability in a semi-infinite domain, owing to a step change in temperature at the boundary. The critical time for the onset of convection in such problems has not been determined accurately by previous studies. We present a solution, based on the dominant mode of the self-similar diffusion operator, which can accurately predict the critical time and the associated unstable wavenumber. This approach is used to explain the instability mechanisms of the critical time and the long-wave cutoff in a semi-infinite domain. The dominant mode solution, however, is valid only for a small parameter range. We extend the analysis by employing the quasi-steady-state approximation (QSSA) which provides accurate solutions in the self-similar coordinate system. For large times, both the maximum growth rate and the most dangerous mode decay as $t^{1/4}$. The long-wave and the short-wave cutoff modes scale as $t^{1/5}$ and $t^{4/5}$, respectively. The instability problem is also analysed in the nonlinear regime by high-accuracy direct numerical simulations. The nonlinear simulations at short times show good agreement with the linear stability predictions. At later times, macroscopic fingers display intense nonlinear interactions that significantly influence both the front propagation speed and the overall mixing rate. A dimensional analysis for typical aquifers shows that for a permeability variation of $1-3000$ mD, the critical time can vary from 2000 yrs to about 10 days while the critical wavelength can be between 200 m and 0.3 m.

1. Introduction

1.1. *Carbon dioxide sequestration*

Carbon dioxide (CO_2) sequestration in deep geological formations has been suggested as a way of reducing greenhouse gas emissions. When CO_2 is injected into an aquifer at a depth greater than 800 m, it forms an immiscible CO_2-rich vapour phase, and a small amount of CO_2 dissolves in the brine (van der Meer 1992). In the temperature and pressure range encountered in geological CO_2 storage, the density of the CO_2-rich vapour phase is less than the density of the brine, but the density of the brine will increase with increasing CO_2 concentration (Ennis-King & Paterson 2003). Several mechanisms for trapping of CO_2 underground should be provided by any suitable injection site. The buoyant CO_2-rich vapour is prevented from rising back to the

† Author to whom correspondence should be addressed.

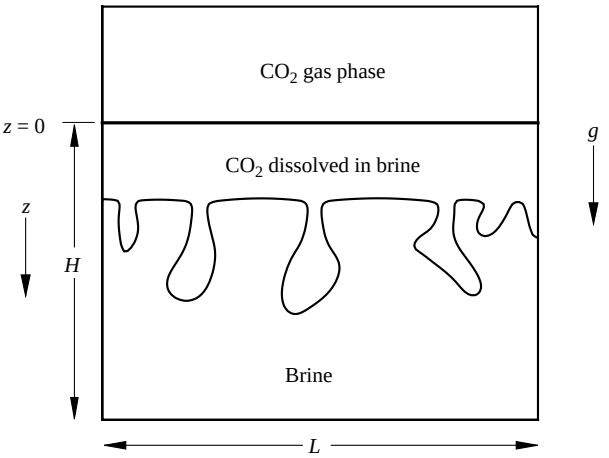

FIGURE 1. Sketch of the CO_2 sequestration process in a simple geometry. A CO_2 gas phase accumulates along the impermeable top boundary. It slowly dissolves into the underlying brine, forming a heavier boundary layer. The resulting gravitational instability leads to the convective transport of CO_2-saturated brine plumes.

surface primarily by an impermeable cap rock referred to as a *hydrodynamic trap* (Bachu, Gunther & Perkins 1994). Another mechanism is dissolution of CO_2 into the brine. The increased density of the CO_2-rich brine prevents the CO_2 from rising. This effect is often referred to as *solution trapping* (Lindeberg & Wessel-Berg 1997; Ennis-King & Paterson 2003). We will discuss the effect of density-driven convection on the effectiveness of this mechanism. Two additional trapping mechanisms, which will not be considered here, are the *residual trapping* in which CO_2 is immobilized by capillary snap-off of bubbles of CO_2 (Kumar *et al.* 2004) and *mineral trapping* in which geochemical reactions convert CO_2 into solid minerals (Hitchon 1996). A hydrodynamic trap is a prerequisite for any storage site, because it prevents the rise of the CO_2-rich vapour during the time required for other trapping mechanisms to immobilize it.

During the injection period, gravity forces will cause the injected CO_2 to accumulate at the top of the reservoir. We model this complex flow process by assuming that the CO_2 forms a layer that is separated from the brine below by a relatively sharp horizontal interface. Across the interface, CO_2 will dissolve into brine to form a diffusive boundary layer that grows with time (Lindeberg & Wessel-Berg 1997). The CO_2-rich brine in this boundary layer is heavier than the underlying brine, and will eventually become unstable, so that fingers of dense CO_2-rich brine propagate downward and transport the aqueous CO_2 away from the interface (see figure 1). This density-driven convection increases the rate of mass transport from the CO_2-rich vapour into the brine, and therefore can reduce the time required for the total dissolution of a CO_2-rich vapour plume by several orders of magnitude (Ennis-King & Paterson 2003).

Numerical simulations by Lindeberg & Bergmo (2003) of the full two-phase problem have shown that the interface between the CO_2-rich vapour and brine remains relatively sharp and is not deflected by the density fingering in the underlying brine, as is shown schematically in figure 1. Both Lindeberg & Bergmo (2003) and Ennis-King & Paterson (2003) show that a local equilibrium between the CO_2-rich vapour and the brine can be assumed at the interface. We assume therefore that the CO_2-rich

vapour layer acts as a horizontal upper boundary, with a constant CO_2 concentration. These authors propose that the gravitational instability can be studied in the context of a finite domain, bounded at the top by a constant concentration boundary, using the Boussinesq approximation. This problem is analogous to thermal convection in a porous medium with insulated boundaries, that is rapidly heated from below, or cooled from the top, at a fixed temperature. Elder (1967, 1968) was among the first to investigate this problem in detail (Diersch & Kolditz 2002). His results suggest that the diffusive layer at the boundary becomes unstable only after an initial period of decaying perturbations. After this critical time, plumes or fingers of hot fluid rise into the porous medium.

1.2. *Previous work on the stability of diffusive boundary layers*

The stability of a concentration base profile to small perturbations depends on the nature of the base state. For steady base states, linear stability theory leads to an algebraic eigenvalue problem (Drazin & Reid 1981; Nield & Bejan 1999). The diffusive boundary layer, however, is a time-dependent base state. A common approach to such stability problems is the use of frozen time coefficients, the so-called quasi-steady-state-approximation (QSSA), (Lick 1964; Robinson 1976). The QSSA is valid, if the growth rate of perturbations is large compared to the growth rate of the diffusive boundary layer. Initially, when the boundary layer grows rapidly, the QSSA is not justified, but it becomes valid for large times, when the base state changes relatively slowly (cf. Tan & Homsy 1987; Riaz & Meiburg 2003*a*, *b*). Gresho & Sani (1971) have shown that the QSSA is not valid for the onset of the instability of a thermal boundary layer in a viscous incompressible fluid.

In order to avoid using the QSSA for small times, several authors have solved the initial-value problem (IVP) numerically for a large number of random initial conditions. However, the solution of the initial-value problem is sensitive to the particular initial conditions, and therefore not unique (Foster 1965). Foster (1965, 1968), Gresho & Sani (1971) and Jhavery & Homsy (1982) solved the IVP for a thermal boundary layer in a viscous incompressible fluid. Caltagirone (1980) and Kaviany (1984) investigated the IVP for a thermal boundary layer in a porous medium due to a step change in temperature. Ennis-King & Paterson (2003) extended the analysis of Caltagirone (1980) to anisotropic porous media, and applied it to the CO_2-sequestration problem. All of these investigations give a wide range of critical times, depending on the particular method of measurement of the growth rate.

The stability of time-dependent base states can be investigated by energy methods (Homsy 1973; Caltagirone 1980). Energy methods give a lower bound for the onset of the instability, but give no information about the growth rate and wavenumber of the most dangerous disturbance.

For unbounded domains, Pritchard (2004) and Ben, Demekhin & Chang (2002) argue that a fundamental limitation on the accuracy of the solution at short times is the assumption of decoupled normal modes in the streamwise direction. Since the disturbances are confined within a narrow diffusive zone, the global Fourier eigenfunctions of the diffusion operator do not provide an optimal basis for streamwise perturbations (Pego & Weinstein 1994). Ben *et al.* (2002) note that the Hermite polynomial-based discrete eigenspectrum of the self-similar diffusion operator is the natural basis for streamwise perturbations in an unbounded domain. This eigenspectrum is the solution of the stability problem for zero wavenumber. The first mode is neutral. It has zero growth rate, whereas the rest of the modes decay with time. Therefore, the first mode becomes dominant after a relatively short time. The

perturbation dynamics can then be projected onto this dominant mode, to increase the growth rate from zero to positive values, for small wavenumbers.

A similar approach is adopted here for the stability analysis in the semi-infinite domain. We use the self-similar transform of the diffusion operator in the inhomogeneous direction with localized eigenfunctions. The zero-wavenumber solution shows that the first mode of the self-similar diffusion operator decays with time, while the rest of the spectrum decays more rapidly. We use this dominant first mode to capture the perturbation dynamics for larger wavenumbers that at later times shift the growth rate from negative to positive values. We show that in contrast to the long-wave instability in an unbounded domain, a critical time, critical wavenumber, and a long-wavelength cutoff characterize the stability problem in the semi-infinite domain.

It is important to note that the dominant mode solution becomes inaccurate for large times and large wavenumbers. For these cases we use the QSSA in self-similar coordinates. We show by comparing with the initial-value problem that the QSSA in this context gives reasonable results. Compared to poor accuracy in the original coordinates, the success of both the QSSA and the IVP in the self-similar coordinate system is due to localized basis functions in the streamwise direction.

In order to analyse the long-term evolution of the unstable modes predicted by the linear stability theory, we carry out high-accuracy direct numerical simulations (DNS) using a vorticity-based formulation (Tan & Homsy 1988). Voss & Sousa (1987) have also carried out numerical simulations of density-driven flows. We use the methodology developed by Ruith & Meiburg (2000) using Fourier–Galerkin decomposition in the lateral direction and compact finite differences in the streamwise direction to solve for the velocity field. For time integration we use a fourth-order Runge–Kutta method. The nonlinear simulations are validated by comparing with the linear stability analysis. Excellent agreement is observed at early times for growth rates associated with individual wavenumbers. The long-time nonlinear behaviour is characterized by complex fingering interactions.

2. Linear stability analysis

2.1. *Governing equations*

The equations describing the Boussinesq-flow in a horizontal porous layer, where gravity points in the positive z-direction, are:

$$\boldsymbol{u} = -\frac{K}{\mu}(\nabla P - \rho g \hat{\mathbf{z}}), \tag{2.1}$$

$$\phi \frac{\partial C}{\partial t} = -\boldsymbol{u}\cdot\nabla C + \phi D \nabla^2 C, \tag{2.2}$$

$$\nabla\cdot\boldsymbol{u} = 0, \tag{2.3}$$

$$\rho = \rho_0 + \Delta\rho C. \tag{2.4}$$

C is the concentration of the heavier fluid normalized to unity, $\boldsymbol{u}=(u, w)$ is the Darcy velocity. K is the permeability, D is the diffusion coefficient, ϕ is the porosity, and μ is the viscosity. The unit vector in the direction of the acceleration due to gravity is $\hat{\mathbf{z}}$. Density ρ is specified as a linear function of concentration and ρ_0 is the density of the lighter fluid. The initial conditions are $\boldsymbol{u}(x, z, t=0)=0$ and $C(x, z, t=0)=0$, and the boundary conditions are given by

$$w(x, z=0, t)=0, \qquad w(x, z=H, t)=0,$$

$$C(x, z = 0, t) = 1, \qquad \left.\frac{\partial C}{\partial z}\right|_{x,z=H,t} = 0.$$

We choose the domain depth H as the length scale, figure 1, and the buoyancy velocity U as the velocity scale. We define the following scaling relations,

$$U = \frac{K\Delta\rho g}{\mu}, \tag{2.5}$$

$$\rho^* = \rho_1 - \rho_0 = \Delta\rho, \tag{2.6}$$

$$P^* = \frac{\mu U H}{K} = \Delta\rho g H, \tag{2.7}$$

$$t^* = \frac{\phi H}{U} = \frac{\phi\mu H}{K\Delta\rho g}. \tag{2.8}$$

Based upon these scaling relationships the non-dimensional equations can be expressed as,

$$\nabla\cdot\boldsymbol{u} = 0, \tag{2.9}$$

$$\boldsymbol{u} = -(\nabla P' - C\hat{\boldsymbol{z}}), \tag{2.10}$$

$$\frac{\partial C}{\partial t} = -\boldsymbol{u}\cdot\nabla C + \frac{1}{Ra}\nabla^2 C. \tag{2.11}$$

A modified pressure $P' = \nabla(P - \rho_0 g\hat{z}/\Delta\rho g H)$ appears in the above equations. The Rayleigh number Ra is the only non-dimensional parameter in the problem defined as,

$$Ra = \frac{UH}{\phi D} = \frac{K\Delta\rho g H}{\phi D\mu}. \tag{2.12}$$

The boundary conditions are,

$$w(x, z = 0, t) = 0, \qquad w(x, z = 1, t) = 0,$$
$$C(x, z = 0, t) = 1, \qquad \left.\frac{\partial C}{\partial z}\right|_{x,z=1,t} = 0.$$

We eliminate pressure by taking the curl of (2.10) and substitute the transverse velocity from the continuity equation. The streamwise velocity, w, and concentration are decomposed into the base state and perturbation components,

$$(w, c)(x, z, t) = (w_o, C_o)(z) + (\hat{w}, \hat{c})(z, t)\mathrm{e}^{\mathrm{i}kx}. \tag{2.13}$$

The base velocity w_o is zero. Although, strictly speaking, a streamwise velocity does not exist since $w_o = 0$, we use this nomenclature to describe the perturbation velocity component in the direction of acceleration due to gravity. The base concentration, C_o, is the solution of (2.11) with $u = 0$ and $\partial/\partial x = \partial^2/\partial x^2 = 0$. The perturbation variables are decomposed into eigenfunctions, which depend on time and the streamwise coordinate, and normal modes in the transverse x-direction with wavenumber k. The linearized perturbation equations can then be expressed as,

$$\left(\frac{\partial^2}{\partial z^2} - k^2\right)\hat{w} = -k^2\hat{c}, \tag{2.14}$$

$$\frac{\partial\hat{c}}{\partial t} - \frac{1}{Ra}\left(\frac{\partial^2}{\partial z^2} - k^2\right)\hat{c} = -\frac{\partial C_o}{\partial z}\hat{w}, \tag{2.15}$$

with boundary conditions,

$$\hat{c}(z=0,t) = \hat{w}(z=0,t)=0, \tag{2.16}$$

$$\left.\frac{\partial \hat{c}}{\partial z}\right|_{z=1,t} = \hat{w}(z=1,t)=0. \tag{2.17}$$

Equation (2.11) admits a streamwise one-dimensional base-state solution, C_o, which is,

$$C_o(z,t) = 1 - \frac{4}{\pi}\sum_{n=1}^{\infty}\frac{1}{2n-1}\sin((n-1/2)\pi z)\exp(-(n-1/2)^2\pi^2 t/Ra).$$

The length $\delta(t)$ over which C_o is non-zero is the so-called 'penetration depth' of the diffusive boundary layer. For $\delta \propto \sqrt{4t/Ra} \ll 1$ the domain can be considered semi-infinite in the positive z-direction, and the base state is given by,

$$C_o(z,t) = 1 - \mathrm{erf}\left(z\sqrt{\frac{Ra}{4t}}\right) \qquad (z \in (0,\infty)), \tag{2.18}$$

with the boundary conditions,

$$C_o(z=0,t) = 1, \tag{2.19}$$

$$C_o(z\to\infty,t) \to 0. \tag{2.20}$$

The problem has now been redefined as the instability of a diffusive boundary layer in a semi-infinite domain. The parameter range over which the results are valid, for the original layer geometry in a finite domain, is given by $\delta \propto \sqrt{4t/Ra} \ll 1$. Note that the semi-infinite domain does not impose any external length scale on the problem. One of the internal length scales in the problem is the time-dependent penetration depth $\delta(t)$. A Rayleigh number based on $\delta(t)$ is itself time dependent, such that a critical Rayleigh number, $Ra_c = Ra(\delta(t_c))$, is merely a function of the critical time, t_c, at which the boundary layer becomes unstable. On the other hand, the Rayleigh number can also be scaled out of the equations by specifying the length scale as a ratio of diffusion to buoyancy velocity, $H = D/U$. In this case, the critical time, t_c, is the only criterion for the onset of instability. For our analysis, we choose to work with the latter, but retain the Rayleigh number, with an arbitrary length scale H, for convenience in comparing the linear stability analysis with the nonlinear results discussed in § 3. In the discussion of the dimensional results (§ 4), we show that the imposed length scale cancels out, so that the choice of length scale is arbitrary.

The perturbation equations, (2.14)–(2.17), can be solved in a straightforward manner by using the quasi-steady-state approximation (QSSA). Earlier investigations have shown that the QSSA gives reasonable results for long times. A fundamental problem with such an approach is that the concentration eigenfunctions are localized in the boundary layer while the eigenfunctions of the operator $\partial^2/\partial z^2, z \in (0,\infty)$ are global modes. Hence, they do not provide an appropriate basis for streamwise perturbations (cf. Chang, Demekhin & Kalaidin 1998). Therefore, in the context of the initial-value problem (IVP), a finite time is required by the global eigenfunctions to represent accurately the localized structure of streamwise perturbations. Since the current problem can have a small critical time, the QSSA as such is ill-suited to the task of resolving the early-time behaviour.

2.2. *Localized eigenmodes of the diffusion operator*

In a semi-infinite domain, we transform the perturbation equations such that the eigenfunctions associated with the streamwise diffusion operator are localized around the base-concentration front. The objective is to achieve considerable improvement in accuracy at small times, even with the QSSA. Following a coordinate transformation to the similarity variable of the base state $\xi = z\sqrt{Ra/4t}$, the base state and the perturbation equations can be expressed as,

$$C_o(\xi) = 1 - \mathrm{erf}(\xi), \tag{2.21}$$

$$\left(\frac{Ra}{4t}\frac{\partial^2}{\partial\xi^2} - k^2\right)\hat{w} = -k^2\hat{c}, \tag{2.22}$$

$$\frac{\partial\hat{c}}{\partial t} - \frac{1}{t}\left(\frac{1}{4}\frac{\partial^2}{\partial\xi^2} + \frac{\xi}{2}\frac{\partial}{\partial\xi} - \frac{k^2 t}{Ra}\right)\hat{c} = \sqrt{\frac{Ra}{\pi t}}\exp(-\xi^2)\hat{w}, \tag{2.23}$$

with boundary conditions,

$$\hat{c}(\xi = 0, t) \;=\; \hat{w}(\xi = 0, t) \;=\; 0, \tag{2.24}$$

$$\hat{c}(\xi = \infty, t) \;=\; \hat{w}(\xi = \infty, t) \;=\; 0. \tag{2.25}$$

Note that the self-similarity applies only to the base concentration. The amplitude and the spatial structure of perturbations are time dependent. The streamwise operator of the perturbation concentration in the transformed coordinate, ξ, is

$$\mathscr{L} = \frac{1}{4}\frac{\partial^2}{\partial\xi^2} + \frac{\xi}{2}\frac{\partial}{\partial\xi} \qquad (\xi \in (0, \infty)). \tag{2.26}$$

We expand the perturbation concentration as,

$$\hat{c}(\xi, t) = \sum_{n=1}^{\infty} A_n(t)\phi_n(\xi), \tag{2.27}$$

with

$$\mathscr{L}\phi_n = \lambda_n\phi_n(\xi) = \lambda_n \mathrm{e}^{-\xi^2}\mathscr{H}_n(\xi) \qquad (n = 1, 2, 3, \ldots). \tag{2.28}$$

The eigenfunctions ϕ_n of $\mathscr{L}$ are the Hermite polynomials $\mathscr{H}_n(\xi)$ in a semi-infinite domain with weight function $\exp(-\xi^2)$ (Robinson 1976). The associated eigenvalues are $\lambda_n = -n$ for $n = 1, 2, \ldots$, and the dominant mode of the perturbation concentration is $\phi_1 = \xi\exp(-\xi^2)$. These eigenfunctions, being localized around the base state, provide an optimal basis for streamwise perturbations in the semi-infinite domain (Pego & Weinstein 1994).

We note from (2.22) and (2.23) that for $k = 0$ and using (2.27), the perturbation amplitude can be expressed as

$$\frac{\mathrm{d}A_n}{\mathrm{d}t} = \lambda_n A_n. \tag{2.29}$$

All modes decay as t^{-n} for $k = 0$, i.e. the flow is stable in the long-wave limit. The perturbation eigenfunction related to the largest eigenvalue, $\phi_1 = \xi\exp(-\xi^2)$, decays as $1/t$.

We solve an initial-value problem with (2.21)–(2.23) to show that the preferred mode of the streamwise perturbations for $k = 0$ is ϕ_1. Figure 2(*a*) shows that the concentration eigenfunction resolves into the dominant mode of $\mathscr{L}$, i.e. $\xi\exp(-\xi^2)$, in a very short time, $(t = \mathscr{O}(1/Ra))$, for any given set of white-noise initial conditions. We show in § 2.4 that the time required for convergence to the first eigenfunction is

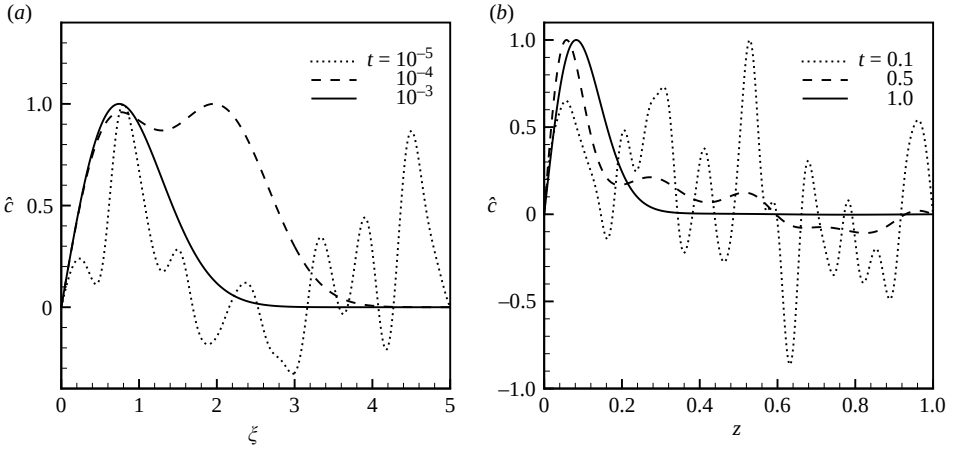

FIGURE 2. Disturbance concentration profile for $Ra = 500$ and $k = 0$ at different times, obtained from, (a) the IVP in the (ξ, t)-coordinate system with (2.21)–(2.23) and (b) the IVP in the (z, t)-coordinate system with (2.14)–(2.18). Random initial conditions are used for both cases. Plot (a) shows that the concentration profile resolves into the correct solution within a very short time, starting from any given set of white-noise initial conditions. For the (z, t)-coordinate system on the other hand, plot (b), convergence is much slower and is strongly dependent on initial conditions.

several orders of magnitude smaller than the critical time for the onset of instability. The IVP in (ξ, t)-coordinates can therefore yield accurate results for short times.

In order to highlight this phenomenon, figure 2(b) plots the perturbation eigenfunction in (z, t)-coordinates, obtained by solving the IVP with (2.14)–(2.18). Although the white-noise initial conditions converge to $\hat{c} \sim z \exp(-z^2 Ra/4t)$, the time required for convergence is several orders of magnitude larger, compared to that in the self-similar coordinates, as shown in figure 2(a). Hence, the small-time dynamics in the (z, t)-coordinate system are obscured during the time it takes for the random initial perturbations to resolve into the dominant mode. This explains why earlier investigations using the IVP in the (z, t)-coordinate system did not produce accurate results. For the (ξ, t)-coordinate system on the other hand, the localized eigenfunctions of $\mathscr{L}$ converge rapidly to the exact solution, thereby giving an accurate disturbance growth rate at small times.

2.3. *Dominant mode solution*

Robinson (1976) used a one-term approximation to the solutions in his QSSA analysis in (z, t)-coordinates, and found that the error is small when compared to expansions using many terms. In the (ξ, t)-coordinates, such a one-term approximation is expected to be even better, because we expand in the eigenfunctions of the streamwise operator. We use the leading-order approximation for $\hat{c}$ from (2.27), substitute it into the IVP (equation (2.23)) and integrate across the domain to obtain,

$$\frac{\mathrm{d}A_1}{\mathrm{d}t} = -\frac{A_1}{t} - \frac{A_1 k^2}{Ra} + \sqrt{\frac{Ra}{\pi t}}\,\langle \exp(-\xi^2)\hat{w}\rangle, \tag{2.30}$$

where,

$$\langle \exp(-\xi^2)\hat{w} \rangle = \frac{\displaystyle\int_0^\infty \exp(-\xi^2)\hat{w}\,\mathrm{d}\xi}{\displaystyle\int_0^\infty \xi \exp(-\xi^2)\,\mathrm{d}\xi}. \tag{2.31}$$

Again, using only the leading-order estimate of $\hat{c}$ to solve for $\hat{w}$, we obtain

$$\left(\frac{\partial^2}{\partial \xi^2} - \frac{4tk^2}{Ra}\right)\hat{w} = -\frac{4tk^2}{Ra} A_1 \xi \exp(-\xi^2). \tag{2.32}$$

This can be solved analytically for $\hat{w}$

$$\hat{w} = -A_1 k \sqrt{\frac{t}{Ra}} \left\{ \exp(2k\sqrt{t/Ra}) \left(\int_0^\xi \xi \exp(-2kx\sqrt{t/Ra} - x^2)\,\mathrm{d}x - B_1 \right) - \exp(-2k\sqrt{t/Ra}) \left(\int_0^\xi \xi \exp(2kx\sqrt{t/Ra} - x^2)\,\mathrm{d}x - B_2 \right) \right\}, \tag{2.33}$$

where

$$\int_0^\xi \xi \exp(-2kx\sqrt{t/Ra} - x^2)\mathrm{d}x = -\tfrac{1}{2}\exp(-2k\xi\sqrt{t/Ra} - \xi^2) - \tfrac{1}{2}k\sqrt{\frac{\pi t}{Ra}}\exp(k^2)\,\mathrm{erf}\left(\xi + k\sqrt{\frac{t}{Ra}}\right), \tag{2.34}$$

and

$$\int_0^\xi \xi \exp(2kx\sqrt{t/Ra} - x^2)\,\mathrm{d}x = -\tfrac{1}{2}\exp(2k\xi\sqrt{t/Ra} - \xi^2) + \tfrac{1}{2}k\sqrt{\frac{\pi t}{Ra}}\exp(k^2)\,\mathrm{erf}\left(\xi - k\sqrt{\frac{t}{Ra}}\right). \tag{2.35}$$

The constants B_1 and B_2 are obtained by satisfying the boundary conditions $\hat{w} = 0$ at $\xi = 0, \infty$. Using this value of $\hat{w}(\xi, t)$, we can then solve numerically the integral in (2.31) to obtain the amplitude equation for the dominant mode with growth rate σ,

$$\frac{\mathrm{d}A_1}{\mathrm{d}t} = \sigma(t;k)\,A_1. \tag{2.36}$$

Equation (2.36) shows that the perturbations grow exponentially. The growth rate $\sigma(t;k)$ is obtained without the QSSA and is expected to yield accurate results.

It is interesting to compare the above development for the semi-infinite case with that of the infinite case analysed by Ben *et al.* (2002). The eigenfunctions of the self-similar operator in the latter case are the full range of Hermite polynomials. The associated eigenvalues are $\lambda_n = -n/2$ for $n = 0, 1, 2, \ldots$, resulting in a neutral mode for the zeroth eigenvalue. In a bounded domain on the other hand, the self-similar operator has eigenfunctions based upon only those Hermite polynomials which satisfy the boundary condition $\hat{c}(\xi = 0, t) = 0$. The associated eigenvalues are $-1, -2, \ldots$; therefore, a neutral mode is not present.

The presence of a zero eigenvalue in the unbounded case implies a long-wave instability ($\sigma = 0$) for $k = 0$ such that the flow is always unstable for small wavenumbers. For the semi-infinite domain on the other hand, the dominant mode decays as t^{-1}, hence $\sigma = -1/t$ for $k = 0$, i.e. the flow is always stable for small

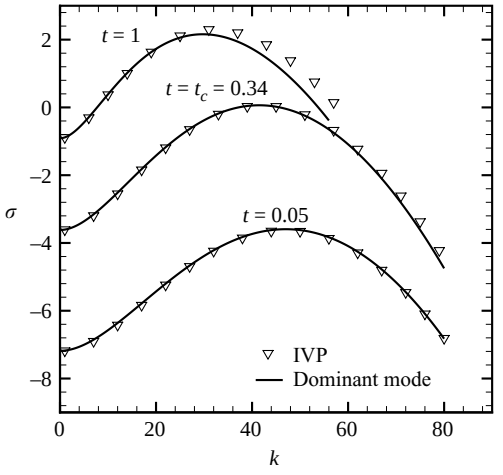

FIGURE 3. Growth rate *vs.* wavenumber curves for $Ra = 500$ computed by the dominant-mode method and the IVP. The flow is stable for small times. The growth rate increases with time to become positive at the critical time t_c and the critical wavenumber k_c. Flow instability increases with time beyond t_c with both short-wave and long-wave cutoffs. Comparison with the IVP shows exact agreement for small times and small wavenumbers.

wavenumbers. A long-wave cutoff therefore exists along with a critical time at which the flow becomes unstable.

The existence of a critical time as a function of the Rayleigh number has been noted previously. However, its exact value as well as the fundamental mechanism have not been given explicitly. Consider the growth rate,

$$\sigma(t;k) = -\frac{1}{t} - \frac{k^2}{Ra} + \frac{k}{\sqrt{\pi}} F(t;k), \tag{2.37}$$

where $F(t;k)$ is computed numerically from (2.31). Since $F(t;k) > 0$, the stabilizing effects come from the first two negative terms on the right-hand side. The first term, $-1/t$, which is due to the non-zero eigenvalue of the dominant mode of $\mathscr{L}$, ensures that $\sigma < 0$ for small times. In physical terms, the flow can become unstable only when the perturbations grow at a rate faster than the decay rate of the first mode of $\mathscr{L}$.

It is important to note that selecting only the first mode to capture the perturbation dynamics cannot be accurate for the entire range of length and time scales of interest, in view of the absence of a neutral mode of $\mathscr{L}$. We show in § 2.4 that the dominant mode solution gives exact results in comparison with the IVP only for small values of $k\sqrt{t/Ra}$. Therefore, we use the QSSA for (2.21)–(2.25) to solve for the growth rates for larger values of $k\sqrt{t/Ra}$. We also show that when the QSSA is used with the governing equations in the self-similar coordinates, accurate results are obtained.

2.4. *Results*

The growth rate *vs.* wavenumber curves given by both the dominant-mode method and the numerical solution of the IVP are shown in figure 3 for different times. High-accuracy numerical simulations of the IVP were carried out for each wavenumber k on a fine computational grid, by using standard methods for one-dimensional problems. The evolution of the maximum value of either the concentration or the

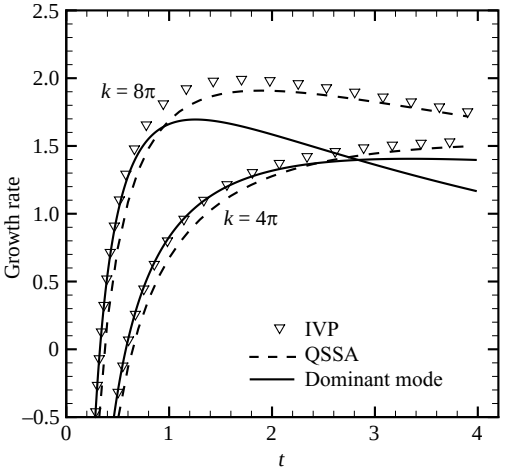

FIGURE 4. Comparison of the dominant-mode method and the QSSA with the initial-value problem for two perturbation wavenumbers at $Ra = 500$. The dominant-mode solution gives exact results for small times, but becomes inaccurate for later times particularly for large wavenumbers. The QSSA on the other hand is reasonably accurate for all times.

velocity eigenfunction forms the basis of the growth rate plotted at a particular time for each wavenumber. Completely stable behaviour is indicated by $\sigma < 0$ for all wavenumbers at early time. A critical time, t_c, is also shown when the growth rate just becomes positive at a critical wavenumber k_c. At larger times, the stability curve displays a maximum growth rate at a corresponding most dangerous wavenumber, along with both a long-wave and a short-wave cutoff. Comparison of the dominant-mode solution with the IVP shows exact agreement for all wavenumbers at small times when $k\sqrt{t/Ra}$ is small. For longer times, the growth rate begins to deviate from the IVP result at larger wavenumbers. However, the critical time and the long-wave cutoff are computed exactly by the dominant-mode solution.

Since the dominant-mode solution does not give accurate results for large values of $k\sqrt{t/Ra}$, we use the QSSA in the self-similar coordinates to compute the growth rates. Figure 4 compares the growth rate as a function of time obtained from the IVP to that computed from the dominant-mode method and the QSSA, for two wavenumbers. The dominant-mode method again gives exact results for small times, but deviates from the IVP solution for large times, particularly for the larger wavenumber. The QSSA, on the other hand, gives reasonably accurate results for all times. This clearly shows that the QSSA in the self-similar coordinates can be employed to obtain reliable results even for short times.

Figures 5(a) and5(b), respectively, show the critical time and the critical wavenumber as a function of the Rayleigh number computed by the dominant-mode method. The critical time varies as Ra^{-1} while the critical wavenumber scales linearly with Ra. Similar scalings have been obtained by Caltagirone (1980), but our analysis eliminates the effect of the initial condition so that we obtain the following relationships for the critical time $t_c \approx 146/Ra$ and the critical wavenumber $k_c \approx 0.07\,Ra$. These relationships apply only when $\sqrt{4t/Ra} \ll 1$. They are not applicable when either Ra is small or t large enough to violate this condition.

The maximum growth rate as a function of time and the corresponding most dangerous mode for various Ra, computed by the QSSA, are shown respectively in

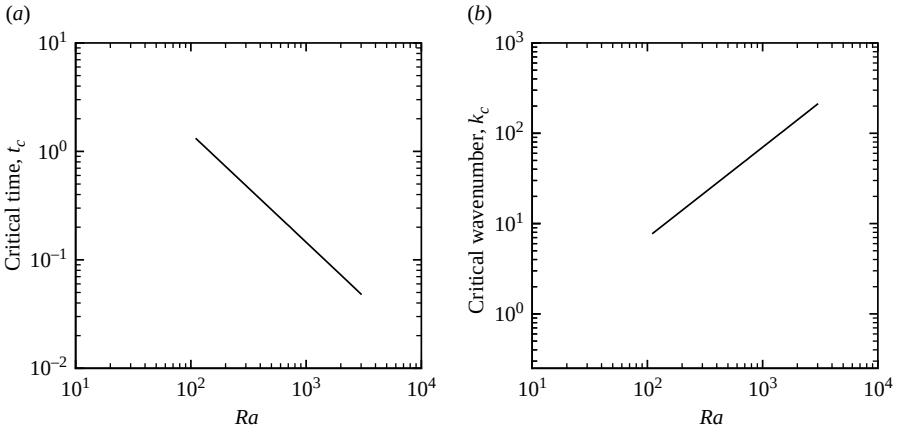

FIGURE 5. (*a*) Critical time *vs. Ra*. (*b*) Critical wavenumber *vs. Ra*, given by the dominant-mode solution. The critical time varies as the $1/Ra$ while the critical wavenumber scales linearly with *Ra*.

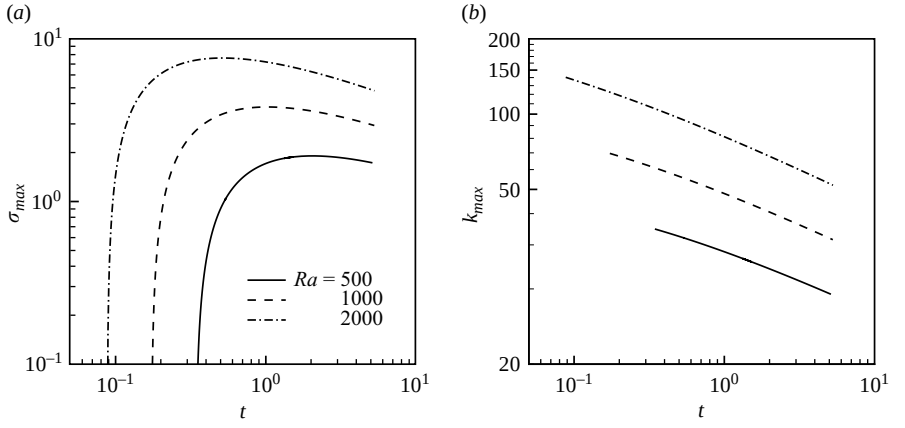

FIGURE 6. (*a*) Maximum growth rate σ_{max} as a function of time, and (*b*) the most dangerous wave-number k_{max} as a function of time, for different Rayleigh numbers. All the results are obtained using the QSSA.

figures 6(*a*) and 6(*b*). The maximum growth rate, σ_{max}, increases rapidly at early time beyond t_c, reaches a maximum value and the late-time evolution shows $\approx t^{1/4}$ decay. The most dangerous wavenumber k_{max} also displays $\approx t^{1/4}$ scaling.

The evolution of the longwave, k_l, and the short-wave cutoff, k_s, is plotted in figure 7. The former decays as $\approx t^{1/5}$, whereas the latter decays much faster as $\approx t^{4/5}$ at long times.

3. Direct numerical simulations

3.1. *Numerical method and validation of the numerical solution*

Nonlinear fingering dynamics govern the long-term flow behaviour. We solve the nonlinear problem with a high-accuracy vorticity-based method proposed by

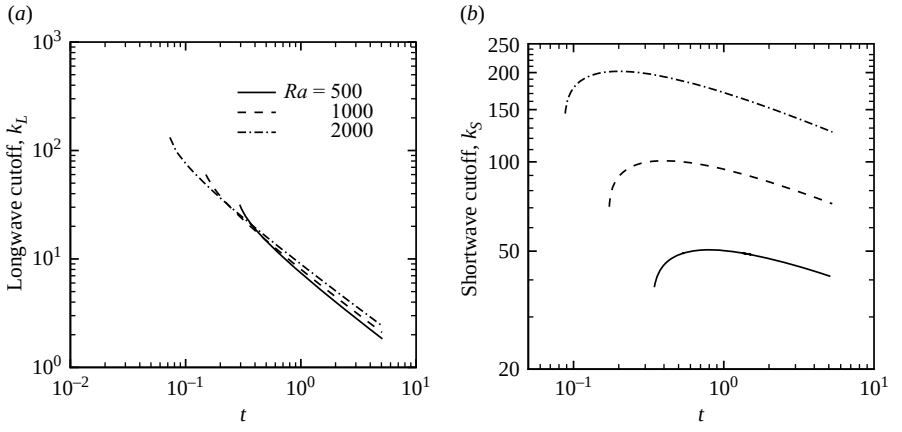

FIGURE 7. (*a*) The long-wave cutoff wavenumber k_L as a function of time for different Rayleigh numbers, computed by the dominant-mode method. k_L behaves similarly for all *Ra* and varies approximately linearly with time. (*b*) The short-wave cutoff k_S computed by the QSSA.

Ruith & Meiburg (2000). This method has been employed successfully to obtain highly accurate results for various miscible-flow problems in porous media (cf. Camhi, Ruith & Meiburg 2000; Riaz & Meiburg 2003*a*, *b*). High-resolution finite-difference simulations have been reported by Otero *et al.* (2004), for high-Rayleigh-number convection in a porous layer of finite depth. They compare the numerical results with analytical heat-flow estimates. We will compare our numerical simulations with the results from the linear stability analysis.

The governing equations used for direct numerical simulations are (2.10) and (2.11). We use a vorticity formulation for (2.10) to eliminate pressure. By taking the curl of (2.10) we obtain,

$$\omega = -\frac{\partial C}{\partial x} = -\nabla^2 \psi, \tag{3.1}$$

where ω is the vorticity and ψ is the streamfunction which is related to velocity as

$$w = \frac{\partial \psi}{\partial x}, \tag{3.2}$$

$$u = -\frac{\partial \psi}{\partial z}. \tag{3.3}$$

Periodicity is assumed in the transverse x-direction, for the vorticity and streamfunction, while symmetry conditions are used for concentration. The boundary conditions are,

$$C(z=0,x,t) = 1, \qquad \frac{\partial C}{\partial z}(z=1,x,t) = 0, \tag{3.4}$$

$$\frac{\partial C}{\partial x}(z,x=0,t) = 0, \qquad \frac{\partial C}{\partial x}(z,x=A,t) = 0, \tag{3.5}$$

$$w(z=0,x,t) = 0, \qquad w(z=1,x,t) = 0, \tag{3.6}$$

$$u(z,x=0,t) = 0, \qquad u(z,x=A,t) = 0. \tag{3.7}$$

The aspect ratio $A = L/H$, where L is the lateral extent of the computational domain and H is the depth (figure 1). The streamfunction $\psi = 0$ on all boundaries while $\omega = 0$

at $x = 0$ and $x = A$. Boundary conditions for vorticity at $z = 0, 1$ can be obtained from (3.1).

We solve the Poisson equation, (3.1), by expanding ω and ψ in Fourier modes in the x-direction. We then solve the resulting ODE for the decoupled z-direction eigenfunctions with sixth-order compact finite differences. For details see Riaz & Meiburg (2003). The velocities are then computed from (3.2) and (3.3) where the derivatives of ψ are evaluated with sixth-order compact finite differences. Time integration of (2.11) is carried out using a standard fourth-order Runge–Kutta method where all the spatial derivatives are again evaluated with sixth-order compact finite differences. The resulting numerical scheme resolves accurately all relevant length and time scales. The initial condition for the concentration is given by (2.18) with a starting time of $t = 0.2$. The initial condition for velocity is $w = u = 0$.

The explicit nature of time integration imposes a strict limit on the time steps. Although stable time steps are given by the CFL condition, we use even smaller time steps, of the order of 10^{-5}, to ensure accuracy. Spatial resolution of the computational grid ranges from 512×512 grid points for small-Rayleigh-number cases to 2048×2048 grid points for larger-Rayleigh-number cases. These fine spatial and temporal resolutions produce converged results. Appropriate grid spacing for different parameter combinations is obtained by consideration of the cutoff mode provided by the linear stability analysis. The grid spacing is chosen such that it is smaller than the cutoff wavelength. Additionally, the divergence of the velocity field is checked throughout to ensure exact mass conservation for a given grid spacing.

Validation of the numerical simulations was performed by comparing the growth rates with those obtained from the linear stability analysis. The numerical simulations are perturbed with pure sinusoidal modes in the transverse direction, superimposed on the initial concentration profile. The growth rate is measured using the norm of vorticity, defined as

$$\overline{\omega}(t) = \int_0^1 \int_0^A \omega(z, x, t)\, \mathrm{d}x\, \mathrm{d}z. \tag{3.8}$$

The growth rate for the numerical simulations is then defined as

$$\sigma_{DNS} = \frac{1}{\Delta t} \ln\left(\frac{\overline{\omega}(t)}{\overline{\omega}(t - \Delta t)}\right). \tag{3.9}$$

Figure 8 shows that the growth rates for the two cases as a function of time for two wavenumbers, although not exactly equal, are in good agreement. The reason for this small discrepancy can be related to the two-dimensional nature of perturbations in the numerical simulations which show a slightly higher rate of growth than the one-dimensional initial-value problem.

3.2. *The flow structure for* $Ra = 4000$

We begin our discussion of the nonlinear dynamics by analysing the concentration contours for $Ra = 4000$. An aspect ratio, $A = 1$ will be used throughout unless noted otherwise. In order to observe the nonlinear behaviour, we perturb the initial concentration with white noise. The initial disturbances are localized within the diffusive zone to avoid unphysical conditions of $C > 1$ or $C < 0$. The wavelength selection mechanism is largely independent of the amplitude and the particular values of the random initial perturbations.

Figure 9 presents the concentration contours at different times. This simulation was carried out with 1024×1024 grid points. At an early time of $t = 1$, figure 9(a) shows

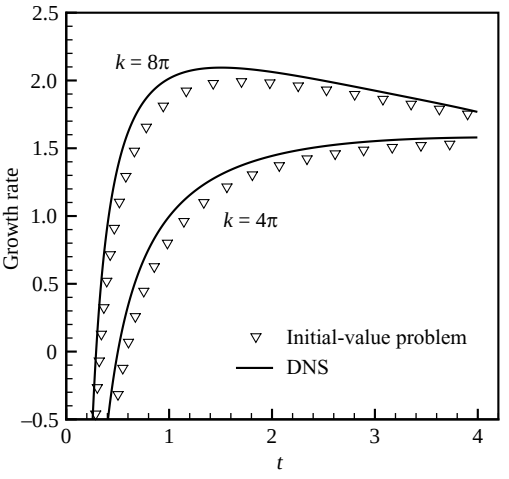

FIGURE 8. Comparison between the nonlinear direct numerical simulations and the initial-value problem in terms of the growth rates of two different perturbation wavenumbers. The two sets of results are in close agreement.

a multitude of competing fingers. The number of fingers is about 24, which is close to 22, predicted by the linear stability analysis. In § 3.3, we will precisely quantify the wavenumber for nonlinear simulations and compare with the linear stability results.

Figure 9(*b*) shows the concentration contours at a later time of $t = 1.8$. The number of fingers is much smaller than that at $t = 1$. This increase in the finger wavelength is primarily due to vigorous nonlinear interactions such as merging and shielding. Fingering instability in this case is reminiscent of viscous and gravitational instability of displacement type flows in porous media (Zimmerman & Homsy 1992; Tchelepi & Orr 1994; Manickam & Homsy 1995). The driving force for instability, i.e. the density gradient, is weakened progressively as the fingers move away from the top boundary. In addition to the diffusive spreading, nonlinear finger interactions tend to further smooth out the concentration gradients of a large number of competing fingers. Consequently, at a later time of $t = 2.3$, shown in figure 9(*c*), some of the smaller fingers disappear owing to diffusive smearing while others merge to form large-scale structures. These larger fingers then travel more or less independently with relatively less interaction with neighbouring fingers. This trend continues for later times, as shown in figure 9(*d*) for $t = 3.8$. Note that at later times, large-scale fingers are connected to the thin diffusive boundary layer at discrete locations, which serve as feeding sites of high-density fluid for the fingers.

Fingering dynamics are revealed by analysis of the vorticity profile that generates the rotational flow responsible for driving the fingers. Figure 10 plots the vorticity field contours for $Ra = 4000$ at $t = 2.3$. The corresponding concentration field is shown in figure 9(*c*). Superimposed on the vorticity field in figure 10 are the streamlines showing the negative (dashed lines) and positive (solid lines) circulation paths. The vorticity field displays a dipole structure of negative (light) and positive (dark) vorticity pairs. Very high vorticity pairs are concentrated at the root of the fingers which act as feeding sites for the finger portions away from the top boundary. The corresponding streamlines show how the fluid is drawn from the sides to flow laterally along the top boundary layer and down through the high-vorticity regions at the finger roots.

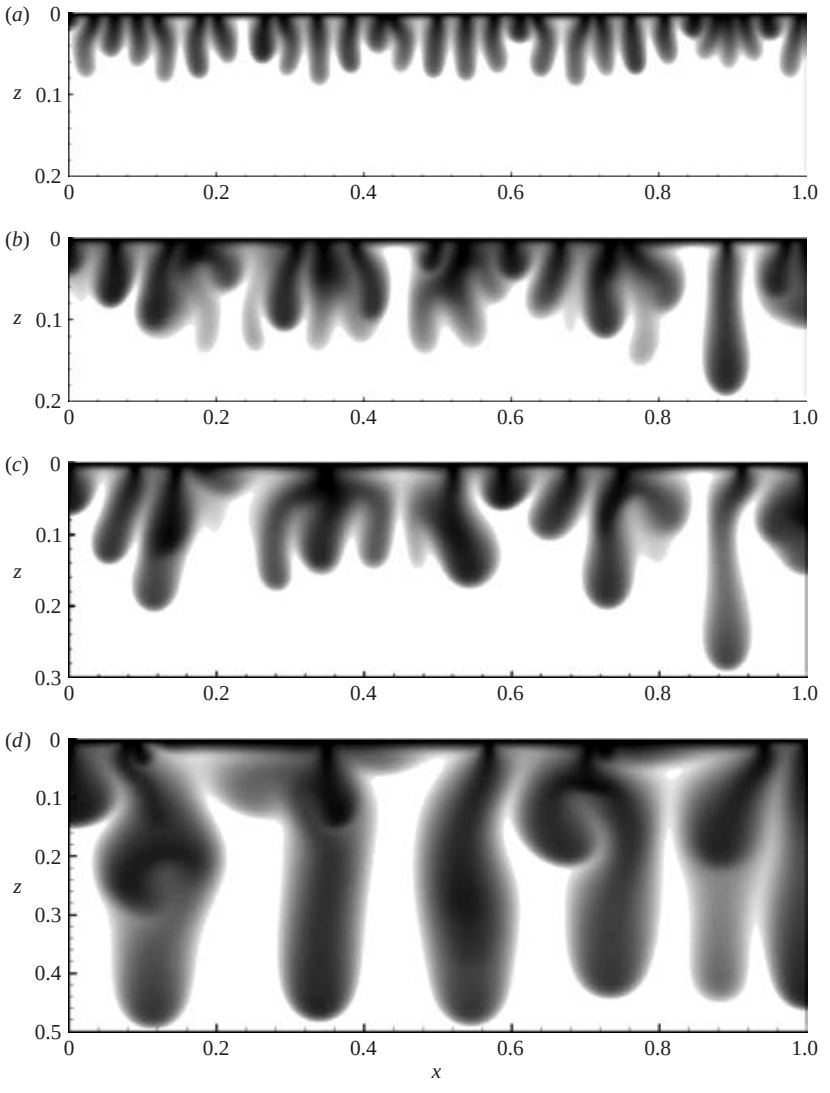

FIGURE 9. Concentration contours at different times for $Ra = 4000$. (*a*) $t = 1$, (*b*) $t = 1.8$, (*c*) $t = 2.3$ and (*d*) $t = 3.8$ A large number of fingers, consistent with the linear stability analysis, develop initially. Nonlinear interactions rapidly reduce the number of fingers and give rise to large-scale structures at later times. The fingers at later times are connected to the top boundary at discrete locations. These connections act as feeding sites of the high-density fluid to the convecting fingers below.

Although the highest vorticity magnitude occurs at the finger roots, the tips of the fingers also display a moderate accumulation of vorticity.

3.3. *Dominant wavenumber of nonlinear flows*

As noted in § 3.2, the early-time wavelength developed by the nonlinear simulations is in close agreement with that predicted by the linear stability analysis. In order to compare the time evolution of the preferred mode of the nonlinear flow, we define a

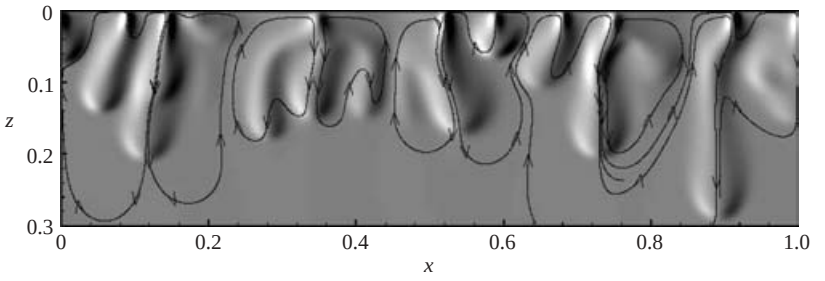

FIGURE 10. Vorticity contours in the background with overlapping streamlines for $Ra = 4000$, $t = 2.3$. Corresponding concentration contours are shown in figure 9(*c*). The vorticity field has a dipole structure that drives the high-density fluid through the fingers. The streamlines show how the fluid travels laterally and then descends through the isolated feeding sites for the fingers. The direction of fluid circulation is shown by the arrows.

dominant mode as,

$$\hat{n} = \frac{\displaystyle\int_0^K k E(k)\,\mathrm{d}k}{\displaystyle\int_0^K E(k)\mathrm{d}k}, \tag{3.10}$$

where $\hat{n}$ is the dominant wavenumber, k is the Fourier mode and $E(k)$ is the energy spectrum associated with the Fourier transform of the vorticity field. We compute $E(k)$ as,

$$\sqrt{E(k;t)} = \int_0^x \left(\int_0^1 \omega(z, x, t)\mathrm{d}z \right) \mathrm{e}^{-\mathrm{i}kx}\,\mathrm{d}x \tag{3.11}$$

The dominant mode $\hat{n}$ is an integral measure of the transverse perturbation spectrum. We have observed the spectrum to be highly localized around the high-energy modes. The magnitude of $\hat{n}$ is a reasonable approximation of the high-energy modes in the spectrum. We have also observed that the energy spectrum is only weakly dependent on the random disturbances introduced as initial conditions. Figure 11 shows the evolution of $\hat{n}$ for various Rayleigh numbers. The most dangerous mode k_{max} from the linear stability analysis is also shown for comparison. We observe a good agreement of $\hat{n}$ with k_{max} for short times. The onset of the nonlinear regime leads to the deviation of the dominant mode away from the most dangerous mode. This deviation from k_{max} is stronger and occurs earlier for higher values of Ra, indicating a stronger influence of nonlinearity for larger Rayleigh numbers.

3.4. *Influence of the Rayleigh number*

Figure 11 shows that the nonlinear behaviour is strongly dependent on the Rayleigh number. In order to estimate the influence of Ra on the flow dynamics, we compare the relatively early-time behaviour at two Rayleigh numbers. Figure 12 plots the concentration contours for $Ra = 1000$ at $t = 2.2$ and $Ra = 8000$ at $t = 1.6$. These simulations employ 512×512 and 2048×2048 grid points, respectively. The concentration front moves much faster for the later case. The $Ra = 1000$ case develops a few large fingers and also shows a substantial amount of diffusive smearing in other regions of the concentration front. The large-scale fingers appear to move independently, without interacting with neighbouring fingers. The $Ra = 8000$ case, on the other hand, develops a vigorous instability that results in complex fingering

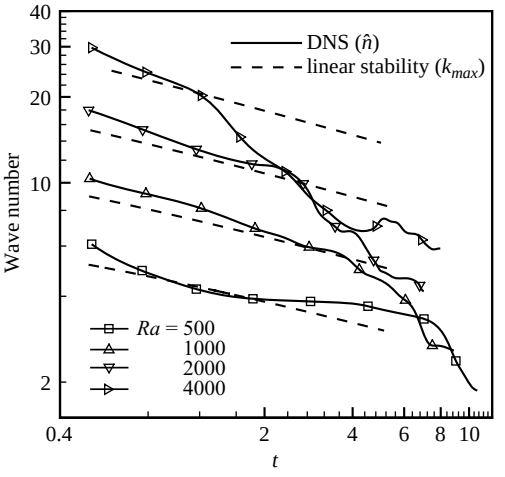

FIGURE 11. The dominant mode of the nonlinear simulations as a function of time for different values of the Rayleigh number. Also shown are the most dangerous modes given by the linear stability analysis. Good agreement is observed between the two for early times. At later times, the onset of nonlinear behaviour leads to a significant deviation from linear results.

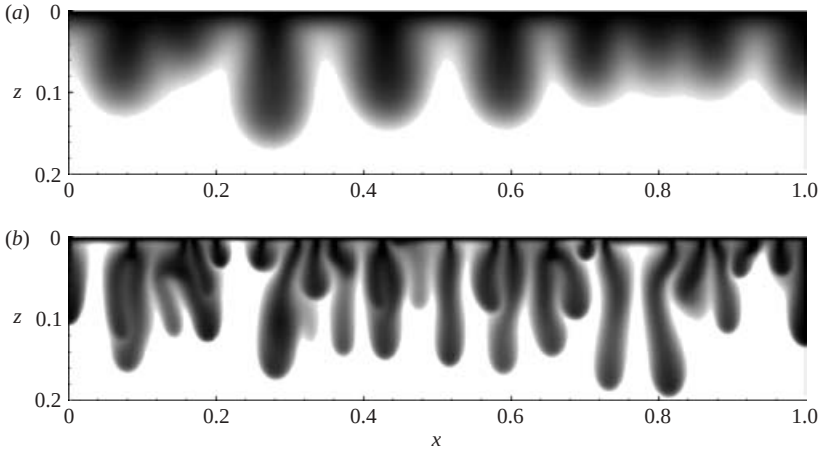

FIGURE 12. Concentration contours for (*a*) $Ra = 1000$, $t = 2.2$ and (*b*) $Ra = 8000$, $t = 1.6$. The larger-Rayleigh-number case is marked by intense nonlinear interaction between competing fingers. The small-Ra case shows larger fingers with a strong diffusive spreading.

structures. Compared to the $Ra = 4000$ case shown in figure 9(*b*) at $t = 0.18$, the $Ra = 8000$ case already shows well-developed discrete feeding sites. Note that new feeding sites develop as the old ones are abandoned. In other regions, multiple fingers can attach to a single feeding site, the nonlinear dynamics then selects one over the others as the preferential flow path.

The complexity of the fingering structures suggest that the long-term fate of the nonlinear competition cannot be predicted from the concentration profiles at earlier times, especially for large Rayleigh numbers. In order to analyse the fingering dynamics at long times, we plot concentration profiles in figure 13 for various Rayleigh numbers at times when the concentration front reaches the bottom boundary. We designate this time as t_b. The small Rayleigh case, $Ra = 1000$ at time $t_b = 8.9$, shows

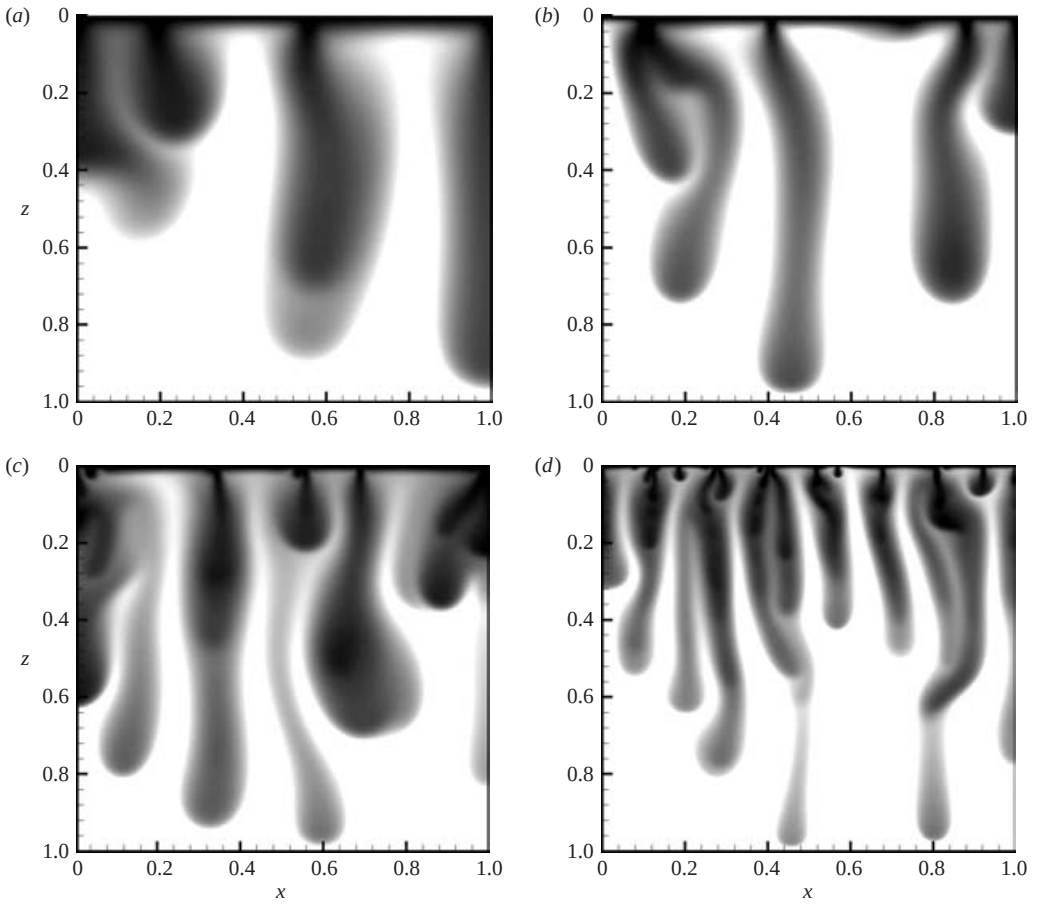

FIGURE 13. Concentration contours at time t_b, when the concentration front reaches the bottom. (*a*) $Ra = 1000$, $t_b = 8.9$. (*b*) $Ra = 2000$, $t_b = 7$. (*c*) $Ra = 4000$, $t_b = 8.0$. (*d*) $Ra = 8000$, $t_b = 8.5$. The late-time dynamics is governed by large-scale fingers. Large-Rayleigh-number cases continue to display vigorous fingering interactions.

that two large fingers survive to reach the bottom boundary. Comparison with figure 12(*a*) shows that the fingering configuration is completely different from that at an earlier time of $t = 2.2$. The $Ra = 2000$ case at $t_b = 7$ displays slightly narrower fingers, with one isolated finger in the middle making it to the bottom boundary, while two other fingers, attached to a single feeding site, are still in competition. For larger-Rayleigh-number cases, $Ra = 4000$, $t_b = 8$ and $Ra = 8000$, $t_b = 8.5$, more fingers reach the bottom boundary. Many of these fingers can be observed to undergo strong interactions while others are in the process of fading out. Figures 13(*c*) and 13(*d*) clearly show that the fading of the fingers is due to the shift in the feeding sites as well as to the lateral pinch-off mechanism, where one diagonally moving finger cuts the fluid supply of the neighbouring finger. A consequence of these fingering interactions is an increase in t_b for larger values of the Rayleigh number, as compared to the small Ra cases. Note that $t_b = 8.9$ for $Ra = 1000$, it decreases to 7 for $Ra = 2000$, but then again increases to 8 for $Ra = 4000$ and then to 8.5 for $Ra = 8000$.

The position of the most advanced section of the concentration front, the tip position, as a function of time is shown in figure 14 for various Rayleigh numbers.

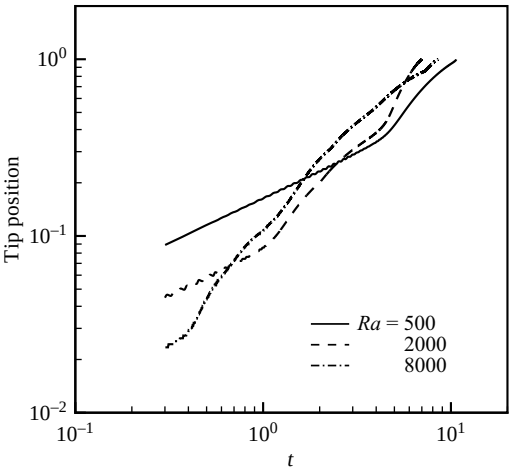

FIGURE 14. The position of the most advanced portion of the front as a function of time for different values of the Rayleigh number. The tip moves faster for larger Rayleigh numbers for early times. Fingering interactions significantly influence the rate of front propagation at later times, particularly for large Ra cases.

For the small $Ra = 500$ case, the front initially propagates as $t^{1/2}$ and then switches to a linear growth for larger times. Higher-Rayleigh-number cases display the diffusive $t^{1/2}$ behaviour for relatively shorter times. The $Ra = 2000$ case displays a faster than linear growth of the tip position at later times. The tip travels quickly for the $Ra = 8000$ case but for a very small initial time. It is clear that by $t = 5$, the tip is moving faster for the $Ra = 2000$ case as compared the $Ra = 8000$ case. Consequently, the time for a finger to reach the bottom boundary is shorter for the $Ra = 2000$ case. As shown by the concentration contours in figure 13, this behaviour is due to a more intense fingering interaction for higher-Rayleigh-number cases, such that the interacting fingers do not allow any one finger to clearly breakaway ahead of the front. For the smaller Ra cases, on the other hand, isolated fingers travel faster owing to the absence of interference from the neighbouring fingers.

4. Discussion

We have analysed the stability of the diffusive boundary layer in a semi-infinite domain. This analysis is applicable when the penetration depth of the diffusive boundary layer, δ, is small relative to the domain thickness, H. The penetration depth at the onset of instability is given in dimensional form as $\delta_c \approx 24\mu D/(K\Delta\rho g)$. We must have $\delta_c \ll H$ for the assumption of the semi-infinite domain to be valid. The dimensional critical time, which is then independent of the length scale, is given by

$$t_c = 146\frac{\phi\mu^2 D}{(K\Delta\rho g)^2}. \tag{4.1}$$

Similarly, we define the dimensional critical wavelength λ_c as

$$\lambda_c = \frac{2\pi\mu D}{0.07K\Delta\rho g}. \tag{4.2}$$

To validate both the linear analysis and the numerical simulations, the predictions of t_c and λ_c should be compared with experimental observations. Unfortunately,

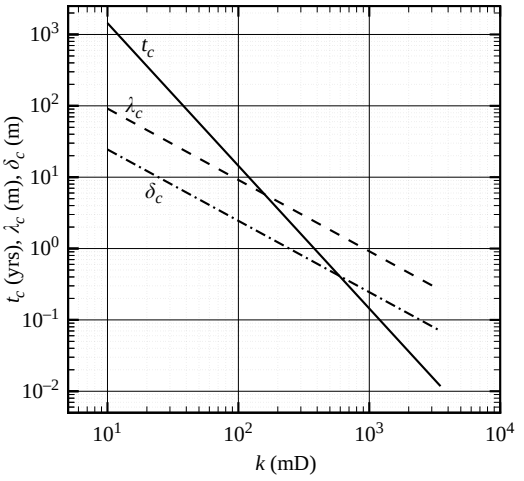

FIGURE 15. Variation with permeability of the critical time, t_c, the critical wavelength, λ_c and the penetration depth at the critical time, δ_c, for $\Delta\rho = 5\,\mathrm{kg\,m^{-3}}$, $\phi = 0.3$, $\mu = 0.5\,\mathrm{cP}$ and $D = 10^{-9}\,\mathrm{m^2\,s^{-1}}$. For this range of permeability variation, t_c varies between 2000 yrs and 10 days while λ_c goes from about 100 m to less than 1 m. The penetration depth δ_c gives information regarding the applicability of our analysis with respect to the layer thickness H, such that $\delta_c \ll H$.

Elder (1968) states only the Rayleigh number of his experiments and does not give all the data necessary to calculate t_c and λ_c. Green & Foster (1975) have reported experiments of a salt solution diffusing into the top of a Hele-Shaw cell. The Rayleigh number in their experiment is $Ra = K\rho g H/(\mu D) = 90\,500$. They do not report the onset time, but give the wavelength of the first observed fingers as $\lambda = 1.8\,\mathrm{mm}$ and note that this may be an overestimate. For the same parameters, our linear stability analysis predicts a critical time of $t_c = 4\,\mathrm{s}$ and a critical wavelength of $\lambda_c = 0.6\,\mathrm{mm}$. The critical wavelength predicted by linear theory is generally smaller than the wavelength first observed, because the fingers are initially not detectable in the experiments. By the time they become observable, they have coarsened to a larger wavelength. Given this experimental limitation on the detection of the critical parameters, high-resolution numerical studies as reported above are valuable because the growth of perturbations can be detected before they become visible.

The critical time and the critical wavelength can vary by orders of magnitude depending on the properties of the geological formation. While viscosity, diffusion and density difference have more or less similar values for typical aquifers, permeability can vary over a large range of values. It therefore introduces the largest variation in the critical time, t_c, and the critical wavelength, λ_c. Figure 15 shows that δ_c decreases from 55 m to about 0.07 m when the permeability increases from 1 mD to 3 D. Hence, our results for the semi-infinite domain will apply to high-permeability layers with a thickness of few tens of metres, but for low-permeability formations the thickness has to be several hundred metres for our results to be applicable. The critical wavelength decreases from $\lambda_c \approx 200\,\mathrm{m}$ to $\lambda_c \approx 0.3\,\mathrm{m}$, while the critical time for the onset of the instability decreases from $t_c \approx 2000\,\mathrm{yrs}$ to $t_c < 10\,\mathrm{days}$.

The critical wavelength, λ_c, is an indication of the length scales that have to be resolved by numerical simulations to capture the convective transport and the resulting solution trapping. In high-permeability reservoirs the fingers are much smaller than

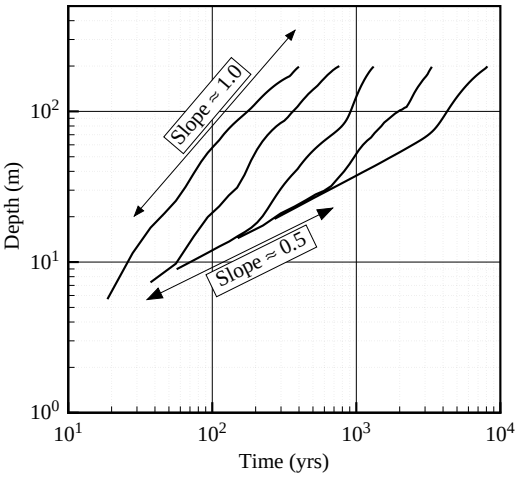

FIGURE 16. The advance of the fastest finger tip is shown until the bottom of the simulation domain is reached. A diffusive, $t^{0.5}$, behaviour is observed at early times, while the fingers advance proportional to t at later times.

the size of grid blocks typically used in reservoir simulations. A numerical study of the high-permeability Sleipner injection site by Lindeberg & Bergmo (2003) shows that a grid block size of 3 cm×4 cm is necessary to capture the initial fingering with a standard reservoir simulator. For field-scale simulation, the grid size has to be increased to 100 m×100 m. Lindeberg & Bergmo (2003) show that this delays the time of onset to 100 years, i.e. two orders of magnitude higher than on the fine grid. Such increases in the onset time may or may not be acceptable, depending on the time scale of storage. More importantly, the failure to resolve the length scales of the critical disturbances at small times may lead to significant errors in the nonlinear regime even if the dominant length scales at long times are coarse enough to be resolved on the chosen grid. Diersch & Kolditz (2002) have investigated the convergence of the Elder problem. They show that even at late times, when most of the structures are large enough to be resolved on a coarse grid, the solution is sensitive to the grid size.

Following the onset of instability, the strength of convective mixing can be determined qualitatively from the speed of the most advanced finger tip, shown in figure 16 for several values of the permeability. All other properties are held fixed at the same values as in figure 15. For all permeability values, the position of the finger tips is initially proportional to $t^{0.5}$. Eventually, however, they accelerate, and the penetration is approximately proportional to t. Note that the late-time rate of advance is similar for all values of permeability. Larger permeability values simply lead to an earlier switch from $t^{0.5}$ to the linear regime. In high-permeability formations, solution trapping is therefore strongly enhanced by convection, and may be the dominant mechanism reducing the amount of the mobile CO_2 phase. To assess the safety and effectiveness of CO_2 storage in high-permeability formations, it is therefore necessary to simulate this convective process accurately.

Heterogeneity is important for the miscible viscous fingering instability (Tchelepi & Orr 1994; Prassad & Simmons 2003; Riaz & Meiburg 2004*b*). Some attempts have been made to model the effect of heterogeneity on the mechanism of this instability (Gounot & Caltagirone 1989), but this remains one of the directions of future research. The fine stratigraphic layering of sedimentary rocks causes strong anisotropy of the

permeability. In general, the vertical permeability may be several orders of magnitude smaller than in the horizontal direction. Ennis-King & Paterson (2003) have shown that anisotropy has an equally strong effect on the critical time and wavelength as the magnitude of the permeability. The analysis developed here can easily be extended to include the effects of anisotropy.

Our analysis does not include the full dispersion tensor which can account for the influence of velocity-induced dispersion (Yortsos & Zeybek 1988; Tchelepi *et al.* 1993). Work by Riaz & Meiburg (2004*a*) suggests that for homogeneous porous media, velocity-induced dispersion is generally equivalent to a slight increase in the level of molecular diffusion. However, dispersion can be expected to play a more important role in heterogeneity dominated flows.

5. Conclusions

Accurate numerical simulation of density fingering over long times at the field scale is one of the main challenges in predicting the movement of CO_2 underground. Our theoretical and numerical results are valuable for understanding the density-driven convection during CO_2 storage in saline aquifers. Our analysis is directly applicable to the thermal instability problem and resolves the issue of the critical time and the critical wavenumber. We also highlight the physical mechanisms of instability that give rise to both the long wavenumber cutoff and the critical time for the onset, in a semi-infinite domain.

The time for the onset of instability can be accurately determined only by the linear stability analysis presented here. Experiments tend to over-predict this time because the disturbances grow to observable fingers only after a finite period following the critical time. For typical aquifers with moderate permeability, the onset time can be as large as hundreds of years. The prediction of the critical wavenumber is crucial in choosing the grid resolution of the numerical simulation. Although the late-time large-scale fingers can be resolved with fewer grid blocks, the errors incurred in ignoring the small-scale dynamics at early times, can have a significant influence on the late time behaviour.

The simplifications necessary to treat the problem theoretically may introduce significant errors when such results are applied to real aquifers. The important assumptions are the homogeneity and isotropy of the porous medium, as well as the assumption of the single-phase flow and the absence of velocity-induced dispersion. The assumption of single-phase flow will break down if capillary forces are significant. Additionally, physical mechanisms related to dissolution, precipitation and geochemical reactions, which are not accounted for in our analysis, can be expected to play a role. Some of these processes may be incorporated in the linear stability analysis, while others can be investigated only with high-resolution nonlinear simulations. The results for the basic gravitational fingering instability presented here, form the basis for investigating the effect and importance of these additional processes.

The authors would like to acknowledge helpful discussions with Dr David Pritchard and Dr Jonathan Ennis-King. This research was supported by the Global Climate and Energy Project and the SUPRI-B, reservoir simulation affiliates program, at Stanford University.

REFERENCES

Bachu, S., Gunther, W. D. & Perkins, E. H. 1994 Aquifer disposal of CO_2: hydrodynamic and mineral trapping. *Energy Conserv. Mgmt* **35**, 269–279.

Ben, Y., Demekhin, E. A. & Chang, H.-C. 2002 A spectral theory for small-amplitude miscible fingering. *Phys. Fluids* **14**, 999.

Caltagirone, J.-P. 1980 Stability of a saturated porous layer subject to a sudden rise in surface temperature: comparison between linear and energy methods. *Q. J. Mech. Appl. Maths* **33**, 47–58.

Camhi, E., Ruith, M. & Meiburg, E. 2000 Miscible rectilinear displacements with gravity override. Part 2. Heterogeneous porous media. *J. Fluid Mech.* **420**, 259.

Chang, H.-C., Demekhin, E. A. & Kalaidin, E. 1998 Generation and suppression of dadiation by solitary pulses. *SIAM J. App. Maths* **58**, 1246.

Diersch, H. J. G. & Kolditz, O. 2002 Variable-density flow and transport in porous media: approaches and challenges. *Adv. Water Res.* **25**, 899–944.

Drazin, P. G. & Reid, W. H. 1981 *Hydrodynamic Stability*. Cambridge University Press.

Elder, J. W. 1967 Transient convection in a porous medium. *J. Fluid Mech.* **27**, 609–623.

Elder, J. W. 1968 The unstable thermal interface. *J. Fluid Mech.* **32**, 69–96.

Ennis-King, J. & Paterson, L. 2003 Role of convective mixing in the long-term storage of carbon dioxide in deep saline formations. *SPE 84344* pp. 1–12.

Foster, T. 1965 Stability of a homogeneous fluid cooled uniformly from above. *Phys. Fluids* **8**, 1249–1257.

Foster, T. 1968 Effect of boundary conditions on the onset of convection. *Phys. Fluids* **11**, 1257–1262.

Gounot, J. & Caltagirone, J.-P. 1989 Stabilité et convection naturelle au sein d'une couche poreuse non homogène. *Intl J. Heat Mass Transfer* **32**, 1131–1140.

Green, L. L. & Foster, T. 1975 Secondary convection in a Hele Shaw cell. *J. Fluid Mech.* **71**, 675–687.

Gresho, P. M. & Sani, R. L. 1971 The stability of a fluid layer subjected to a step change in temperature: Transient vs. frozen time analysis. *Intl J. Heat Mass Transfer* **14**, 207.

Hitchon, B. 1996 Aquifer disposal of carbon dioxide: hydrodynamic and mineral trapping-proof of concept. *Tech. Rep*. Alberta Research Council.

Homsy, G. M. 1973 Global stability of time-dependent flows: impulsively heated or cooled fluid layers. *J. Fluid Mech.* **60**, 129–139.

Jhavery, B. S. & Homsy, G. M. 1982 The onset of convection in fluid layer heated rapidly in a time-dependent manner. *J. Fluid Mech.* **114**, 251.

Kaviany, M. 1984 Onset of thermal convection in a saturated porous medium: experiment and analysis. *Intl J. Heat Mass Transfer* **27**, 2101–2110.

Kumar, A., Noh, M., Pope, G. A., Sepehrnoori, K., Bryant, S. & Lake, L. 2004 Reservoir simulation of CO_2 storage in deep saline aquifers. *SPE 89343* .

Lick, W. 1964 The instability of a fluid layer with time-dependent heating. *J. Fluid Mech*. **21**, 565–576.

Lindeberg, E. & Bergmo, P. 2003 The long-term fate of CO_2 injected into an aquifer. In *Greenhouse Gas Control Technologies* (ed. J. Gale & Y. Kaya), vol. 1, pp. 489–495. Elsevier.

Lindeberg, E. & Wessel-Berg, D. 1997 Vertical convection in an aquiver column under a gas cap of CO_2. *Energy Conserv. Mgmt* **38**, SS229–SS234.

Manickam, O. & Homsy, G. M. 1995 Fingering instability in vertical miscible displacement flows in porous media. *J. Fluid Mech.* **288**, 75.

van der Meer, L. G. H. 1992 Investigations regarding the storage of carbon dioxide in aquifers in the Netherlands. *Energy Conserv. Mgmt* **33**, 611–618.

Nield, D. A. & Bejan, A. 1999 *Convection in Porous Media*, 2nd edn. Springer.

Otero, J., Dontcheva, L. A., Johnston, H., Worthing, R. A., Kurganov, A., Petrova, G. & Doering, C. R. 2004 High-Rayleigh-number convection in a fluid-saturated porous layer. *J. Fluid Mech.* **500**, 263–281.

Pego, R. L. & Weinstein, M. I. 1994 Asymptotic stability of solitary waves. *Commun. Math. Phys.* **104**, 305.

Prassad, A. & Simmons, C. T. 2003 Unstable density driven flow in heteroheneous porous media: a stochastic study of the Elder [1967*b*] 'short heater' problem. *Water Resources Res.* **39**, 1–21.

Pritchard, D. 2004 The instability of thermal and fluid fronts during radial injection in porous media. *J. Fluid Mech.* **508**, 133.

Riaz, A. & Meiburg, E. 2003*a* Radial source flows in porous media: linear stability analysis of axial and helical perturbations in miscible displacements. *Phys. Fluids* **15**, 938.

Riaz, A. & Meiburg, E. 2003*b* Three-dimensional miscible displacement simulations in homogeneous porous media with gravity override. *J. Fluid Mech.* **494**, 95.

Riaz, A. & Meiburg, E. 2004*a* Linear stability of radial displacements in porous media: influence of velocity-induced dispersion and concentration-dependent diffusion. *Phys. Fluids* **16**, 3592.

Riaz, A. & Meiburg, E. 2004*b* Vorticity interaction mechanisms in variable-viscosity heterogeneous miscible displacements with and without density contrast. *J. Fluid Mech.* **517**, 1.

Robinson, J. L. 1976 Theoretical analysis of convective instability of a growing horizontal thermal boundary layer. *Phys. Fluids* **19**, 778–791.

Ruith, M. & Meiburg, E. 2000 Miscible rectilinear displacements with gravity override. Part 1. Homogeneous porous medium. *J. Fluid Mech.* **420**, 225.

Tan, C. T. & Homsy, G. M. 1987 Stability of miscible displacements in porous media: radial source flow. *Phys. Fluids* **30**, 1239.

Tan, C. T. & Homsy, G. M. 1988 Simulation of nonlinear viscous fingering in miscible displacement. *Phys. Fluids* **31**, 1330.

Tchelepi, H. A. & Orr, F. M. Jr 1994 Interaction of viscous fingering, permeability inhomogeneity and gravity segregation in three dimensions. *SPE Res. Engng* p. 266.

Tchelepi, H. A., Orr, F. M. Jr, Salin, D. & Woumeni, R. 1993 Dispersion, permeability heterogeneity and viscous fingering: acoustic experimental observations and particle tracking simulations. *Phys. Fluids* **5**, 1558.

Voss, C. I. & Sousa, W. R. 1987 Variable density flow and solute transport simulation of regional aquifers containing a narrow freshwater–saltwater transition zone. *Water Resources Res* **28**, 1851.

Yortsos, Y. C. & Zeybek, M. 1988 Dispersion driven instability in miscible displacement in porous media. *Phys. Fluids* **31**, 3511.

Zimmerman, W. B. & Homsy, G. M. 1992 Viscous fingering in miscible displacements: unification of effects of viscosity contrast, anisotropic dispersion and velocity dependence of dispersion on nonlinear finger propagation. *Phys. Fluids* **4**, 2348.